Article:
Beckert, A, Grimm, M, Hermans, RI et al. (8 more authors) (2022) Precise determination of the low-energy electronuclear Hamiltonian of LiY1−x HoxF4. Physical Review B, 106 (11). 115119. ISSN 2469-9950

https://doi.org/10.1103/physrevb.106.115119

Precise determination of low energy electronuclear Hamiltonian for $LiY_{1-x}Ho_xF_4$

A. Beckert,[1,2,*] M. Grimm,[2,3] R. I. Hermans,[4] J. R. Freeman,[5] E. H. Linfield,[5]
A. G. Davies,[5] M. Müller,[3] H. Sigg,[1] S. Gerber,[1] G. Matmon,[1] and G. Aeppli[1,2,6]

[1] *Laboratory for Micro and Nanotechnology, Paul Scherrer Institut, CH-5232 Villigen PSI, Switzerland*
[2] *Laboratory for Solid State Physics, ETH Zurich, CH-8093 Zurich, Switzerland*
[3] *Condensed Matter Theory Group, LSM, NES, Paul Scherrer Institut, CH-5232 Villigen PSI, Switzerland*
[4] *London Centre for Nanotechnology, University College London, 17-19 Gordon Street, London WC1H 0AH, United Kingdom*
[5] *School of Electronic and Electrical Engineering, University of Leeds, Woodhouse Lane, Leeds LS9 2JT, United Kingdom*
[6] *Institute of Physics, EPF Lausanne, CH-1015 Lausanne, Switzerland*

(Dated: September 14, 2022)

The insulating rare-earth magnet $LiY_{1-x}Ho_xF_4$ has received great attention because a laboratory field applied perpendicular to its crystallographic $c-$axis converts the low energy electronic spin Hamiltonian into the transverse field Ising model. The mapping between the real magnet and the transverse field Ising model is strongly dependent on the exact nature of the low energy Hamiltonian for the material, which can be determined by optical spectroscopy in the dilute limit. The energies of the eigenstates are in the difficult THz regime, and here we use complementary methods to directly measure the lowest crystal-field levels of $LiY_{1-x}Ho_xF_4$, including nuclear hyperfine substructure, with more than 10 times higher resolution than previous work. We are able to observe splittings due to the ^{6}Li and ^{7}Li isotopes, as well as non-equidistantly spaced Ho ($I = 7/2$) hyperfine transitions originating from dipolar and quadrupolar hyperfine interactions. We provide refined crystal field parameters and extract the dipolar and quadrupolar hyperfine constants $A_J = 0.02703 \pm 0.00003\,\mathrm{cm}^{-1}$ ($810.3 \pm 0.9\,\mathrm{MHz}$) and $B = 0.04 \pm 0.01\,\mathrm{cm}^{-1}$ ($1.2 \pm 0.3\,\mathrm{GHz}$), respectively. Thereupon we determine all crystal-field energy levels and magnetic moments of the $^5I_8$ ground state manifold, including the (non-linear) hyperfine corrections. The latter match the measurements. The scale of the non-linear hyperfine corrections sets an upper bound for the inhomogeneous line widths that would still allow for unique addressing of a selected hyperfine transition *e.g.* for quantum information applications. Additionally, we establish the far-infrared, low-temperature refractive index of $LiY_{1-x}Ho_xF_4$.

I. INTRODUCTION

The $LiY_{1-x}Ho_xF_4$ dilution series has been a fertile venue for quantum phenomena, including single ion tunneling in the very dilute limit [1], quantum phase transitions to both ferromagnetic [2, 3] and quantum glass states [4–6], ferromagnetic domain wall tunneling [7], quantum Griffiths effects [8], as well as an entangled low temperature state [9] with extraordinarily sharp low frequency collective modes revealed by spectral hole burning [10–12]. In addition, over two decades ago, experiments [13] on the material showed the potential of quantum annealing for solving optimization problems, and so spawned the adiabatic quantum computing subtopic of quantum technologies.

The success of the experiments on $LiY_{1-x}Ho_xF_4$ depends on the isostructural nature of the dilution series from ferromagnetic $LiHoF_4$ to non-magnetic $LiYF_4$ as well as the relatively small laboratory fields which convert the effective low energy electronic Hamiltonian into the "classic" transverse field Ising model (for a review see Ref. [14]). While this model captures much of the essential physics also at zero applied field where the dipolar interaction between Ho ions can induce internal transverse fields, it does not suffice for a detailed description even of the quantum phase transition in pure $LiHoF_4$, a fact recognized long ago both by the original experimentalists [3] as well as theorists [15, 16], let alone the hole-burning [10–12] at intermediate x. In particular, the Ho atoms carry nuclear spins $I = 7/2$ with a large hyperfine (HF) coupling to the electronic moments. Furthermore, laboratory fields mix relatively low-lying crystal field (CF) states to split the ground state into the two levels of the simple transverse field Ising model, and so to lowest order the transverse field in the model is not linear but rather quadratic, with higher order corrections, in the laboratory field. Finally, in addition to the strongly coupled nuclear spins on the rare earth atoms themselves, there are much more weakly coupled nuclear spin baths due to the Li and F ligands. The mapping of $LiY_{1-x}Ho_xF_4$ to the transverse field Ising model is determined by the exact nature of the low energy CF and hyperfine Hamiltonian, implying a need for precise spectroscopy to underpin further progress concerning the quantum statistical mechanics of $LiY_{1-x}Ho_xF_4$. Owing to the challenges of experiments in the terahertz (THz) regime where the relevant CF excitations are found, comprehensive high-resolution data for $LiY_{1-x}Ho_xF_4$ have not been available so far [17–20], although we have recently combined optical comb synthesis and a software controlled modulator to obtain ultra-high resolution data for the HF-split lowest CF excitation near 0.2 THz [21]. Here we integrate

* adrian.beckert@psi.ch

theory with low-temperature THz time-domain spectroscopy (TDS) and synchrotron-based ultra-high resolution Fourier transform infrared (FTIR) spectroscopy (Sec. II) to re-examine the transitions between the three lowest-lying CF levels of the $^5I_8$ ground-state manifold of $LiY_{1-x}Ho_xF_4$. In particular, we use previous treatments of nuclear spins coupled to electronic CF states (*e.g.*in Refs. [22, 23]) up to second order in the dipolar interaction, and to first order in the quadrupolar coupling in Sec. III to describe our data. We also include energy shifts due to ^{6}Li and ^{7}Li isotopes. We extract CF parameters by combining our data with CF energy measurements of the $^5I_8$ manifold from Ref. [20], which enables us to refine the dipolar HF interaction constant A_J in Sec. IV. Based on the resulting CF parameters, we predict all $^5I_8$ CF energies and their magnetic moments. The high instrumental resolution allows us also to determine the quadrupolar HF constant B. Using B and A_J, we infer non-equidistant HF corrections of the three CF levels involved in our measurements, including the ground state. We provide an approximation of these HF corrections based on our measurement results, which corroborate our numerical simulation. We conclude in Sec. IV by discussing the implications of non-equidistant HF corrections on unambiguous addressing of specific HF transitions *e.g.* for quantum information applications. In the Appendix A we provide a refractive index measurement of $LiY_{1-x}Ho_xF_4$ from 70 to 5 cm^{-1} corresponding to ~ 2 THz to the sub-THz range; these data are useful for planning the design of future optical experiments and devices. A summary and an outlook are found in Sec. V.

II. EXPERIMENTAL SETUP

A. Sample

We study three commercially-available $LiY_{1-x}Ho_xF_4$ single crystals at low doping concentrations of $x = 1\%$, 0.1%, and 0.01%. Ho^{3+} ions substitute for the Y^{3+} ions in the Scheelite crystal structure (space group C_{4h}^6) of $LiYF_4$ having the local point symmetry group S_4. For an overview of the physical properties and studies of $LiY_{1-x}Ho_xF_4$ as a function of doping concentration x, external magnetic fields and temperature we refer to Refs. [20, 24].

The crystal dimensions along the light propagation direction are chosen such that transmission is optimized for each x. Samples were mounted on the cold finger of a continuous-flow liquid-helium cryostat. The THz light was linearly polarized. The sample was oriented with the crystallographic $c-$axis parallel (8.2 → 8.3) or perpendicular (8.1 → 8.2, 8.1 → 8.3) to the magnetic field component, while the photon propagation direction was perpendicular to c. All reported temperatures denote the nominal values at the cryostat cold finger.

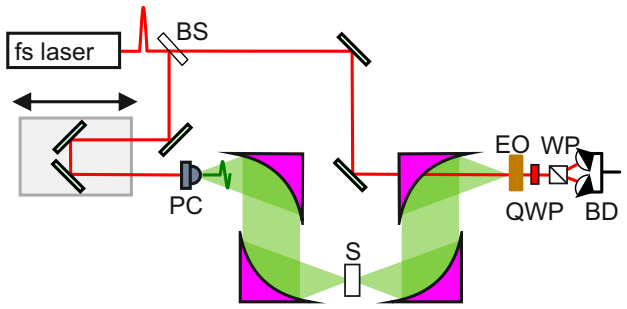

FIG. 1. Schematic of the time-domain spectroscopy setup showing the femtosecond (fs) laser, the beam-splitter (BS), a photo-conductive (PC) antenna, the sample (S), a ZnTe electro-optic (EO) sampling crystal, a quarter-wave plate (QWP), a Wollaston prism (WP) and balanced photo-diodes (BD) for detection.

B. Experimental methods

We use two different methods: First, TDS was conducted on $LiY_{1-x}Ho_xF_4$ ($x = 0.1\%$) for wavenumbers $\tilde{\nu} < 10\,cm^{-1}$ (300 GHz), as well as for refractive-index measurements of the $x = 1\%$ crystal for $\tilde{\nu} \leq 70\,cm^{-1}$ (2.1 THz). Figure 1 shows a schematic of the custom experimental setup, which is based on an 800 nm laser, delivering 100 fs pulses at 80 MHz repetition rate. The beam is split, directing 250 mW through a variable delay line. This fraction of the laser is focused onto a low-temperature grown GaAs photo-conductive emitter with a 100 μm electrode gap (biased at 100 V, 7.3 kHz) that generates a linearly polarized single-cycle THz pulse. The THz pulse is then collected from the back of the emitter substrate with a Si hyper-hemispheric lens and focused on the sample with a parabolic mirror. Thereafter, the transmitted beam is refocused onto a 2 mm thick ZnTe crystal for electro-optic sampling. In this detection scheme, the THz branch is overlapped with the 800 nm branch. As a function of delay time, the polarization change of the transmitted 800 nm light is then proportional to the instantaneous THz field in the ZnTe crystal. The signal is measured using balanced photodiodes and a lock-in amplifier referenced to the emitter bias frequency. Fourier transforms of the delay scans then yield the spectra.

Second, ultra-high resolution FTIR spectroscopy was conducted on $LiY_{1-x}Ho_xF_4$ ($x = 0.01\%$) for $\tilde{\nu} > 15\,cm^{-1}$ (450 GHz) using a custom-built Bruker FTIR spectrometer with 0.00077 cm^{-1} (23 MHz) resolution. A He-flow cryostat for low-temperature measurements was fitted to the spectrometer. The Swiss Light Source at the Paul Scherrer Institut, Switzerland, provides high-brilliance and strongly polarized far-infrared (FIR) radiation. Reference [25] provides more details about the FTIR instrument. The unique combination of a low-temperature, ultra-high resolution spectrome-

ter and FIR/THz synchrotron radiation allowed us to measure the absorbance spectra with a resolution of up to $10^{-3}\,\mathrm{cm}^{-1}$ (30 MHz), which is more than an order of magnitude higher than previously reported direct [19, 20, 26, 27] and at least double the resolution of indirect measurements [20, 28–30].

The THz response of the holmium ions (Ho^{3+}) in the $LiYF_4$ matrix is characterized by referencing the sample absorption at low temperature to a higher temperature measurement. This ensures that both the background absorption of the crystal host and temperature-independent reflections from the sample and the experimental setup are removed. Therefore, we show absorbance spectra $A(\tilde{\nu}) = \mathrm{Log}_{10}[I_0(\tilde{\nu})/I(\tilde{\nu})]$ as a function of wavenumber $\tilde{\nu}$ [cm^{-1}], with $I(\tilde{\nu})$ [$I_0(\tilde{\nu})$] denoting the wavenumber-dependent sample (reference) transmission.

III. CRYSTAL FIELD TRANSITIONS WITH HYPERFINE INTERACTIONS

Our high-resolution instruments enable us to resolve the HF structure of the measured CF states to high precision; analysis methods which take advantage of this structure are described in Ref. [31]. We turn now to the theoretical understanding of the HF corrections to the measured CF states. In this manuscript we denote a transition from an initial CF state i to a final state f by $i \rightarrow f$. Further, we label the ${}^5I_8$ ground state manifold states $8.n$ according to their CF energy E_n: the ground state ($8.1, E_1 = 0$) is a doublet (under time-reversal symmetry) and carries $\Gamma_{3,4}$ symmetry, the first excited (8.2) and second excited (8.3) states have Γ_2 symmetry at $E_2 = 6.8\,\mathrm{cm}^{-1}$ (205 GHz) and $E_3 = 23.3\,\mathrm{cm}^{-1}$ (699 GHz), respectively. We denote the CF symmetries (irreducible representations) by $\Gamma_j,\ j \in \{1,2,3,4\}$, using standard conventions. Individual HF states are labelled as $|8.n^\sigma, m_z\rangle \equiv |8.n^\sigma\rangle \otimes |m_z\rangle$, where $\sigma = -1$ ($\sigma = +1$) denotes the Γ_3 (Γ_4) state if the $n-$th level belongs to a doublet. m_z is the nuclear spin projection onto the crystallographic $c-$axis in the unperturbed electron-nuclear wavefunction.

A. Hyperfine interaction in perturbation theory

Within the lowest $J-$multiplet, the electrons of each Ho^{3+} ion ($J = 8$) couple to their nuclear spin ($I = 7/2$) via the dipolar and quadrupolar HF interactions

$$\begin{aligned} H_{\mathrm{HF}} =& H_{\mathrm{HF,dip}} + H_{\mathrm{HF,quad}} \\ =& A_J\,\vec{J}\cdot\vec{I} + \frac{B}{2I(2I-1)J(2J-1)}\Big(3(\vec{J}\cdot\vec{I})^2 \\ &+ \frac{3}{2}(\vec{J}\cdot\vec{I}) - I(I+1)J(J+1)\Big), \end{aligned} \tag{1}$$

with the dipolar and quadrupolar coupling constants A_J and B, respectively [32, 33]. We consider effects of A_J up to second order and B to first order because of the relative size of these terms. We neglect HF corrections due to coupling of the nuclear electric quadrupole moment to the electric field gradient. Using the literature value in Ref. [34], this effect is estimated to be an order of magnitude smaller than the terms in Hamiltonian (1).

Using perturbation theory as in Ref. [33], the ground-state energy corrections $\delta_{8.1^\sigma,m_z}$ of the states $|8.1^\sigma, m_z\rangle$ are

$$\begin{aligned} &\delta_{8.1^+,+m_z} = \delta_{8.1^-,-m_z} = A_J\,\langle 8.1^+|J_z|8.1^+\rangle\, m_z \\ &+ \sum_{j\in\Gamma_1} \frac{A_J^2}{4\Delta E_{1j}}\Big[|\langle 8.j|J_+|8.1^+\rangle|^2\big(I(I+1) - m_z(m_z-1)\big)\Big] \\ &+ \sum_{j\in\Gamma_2} \frac{A_J^2}{4\Delta E_{1j}}\Big[|\langle 8.j|J_-|8.1^+\rangle|^2\big(I(I+1) - m_z(m_z+1)\big)\Big] \\ &+ \sum_{\substack{j\in\Gamma_{3,4}\\ j\neq 1}} \frac{A_J^2}{\Delta E_{1j}}\Big[|\langle 8.j^+|J_z|8.1^+\rangle|^2 m_z^2\Big] \\ &+ \frac{B\,\langle 8.1^+|3J_z^2 - J(J+1)|8.1^+\rangle}{4I(2I-1)J(2J-1)}(3m_z^2 - I(I+1)), \end{aligned} \tag{2}$$

and the corrections of the first two excited electronic states ($n = 2, 3$) are

$$\begin{aligned} &\delta_{8.n,\pm m_z} = \sum_{\substack{j\in\Gamma_2\\ j\neq n}} \frac{A_J^2}{\Delta E_{nj}}|\langle 8.j|J_z|8.n\rangle|^2 m_z^2 \\ &+ \sum_{j\in\Gamma_{3,4}} \frac{A_J^2}{2\Delta E_{nj}}\Big[|\langle 8.j^+|J_+|8.n\rangle|^2\big(I(I+1) - m_z(m_z+1)\big)\Big] \\ &+ \frac{B\,\langle 8.n|3J_z^2 - J(J+1)|8.n\rangle}{4I(2I-1)J(2J-1)}(3m_z^2 - I(I+1)). \end{aligned} \tag{3}$$

Here $\Delta E_{nj} = E_n - E_j$ is the energy difference between the CF levels $|8.n\rangle$ and $|8.j\rangle$. The sums run over all CF states $|8.j\rangle$ carrying the irreducible representations $\Gamma_i,\ i \in \{1,2,3,4\}$. From now on, we use the abbreviation $\lambda_n/2$ for the prefactor of the HF corrections $\propto m_z^2$ of the CF states $8.n$.

These perturbative corrections are sufficient to interpret the HF spectrum of the 8.1, 8.2 and 8.3 states. Due to the absence of external magnetic fields, then by Kramers' theorem all HF states are doubly degenerate with their time-reversed state (under time-reversal: $m_z \rightarrow -m_z$, $\sigma \rightarrow -\sigma$). The electronic doublet 8.1, which is Ising-like with a moment along the crystallographic $c-$axis (due to the S_4 site symmetry [24]), experiences a dominant first order shift $\propto \sigma A_J m_z$ that leads to an equidistant HF splitting into eight HF Kramers doublets. In the lowest ($\sigma m_z = -7/2$) and highest ($\sigma m_z = +7/2$) of these HF states the electronic and magnetic moments are anti-aligned and aligned, respectively. The singlets do not undergo a first-order HF shift in A_J due to their vanishing moment. Within a single CF state, the equidistance of the HF energies is broken by the second-order

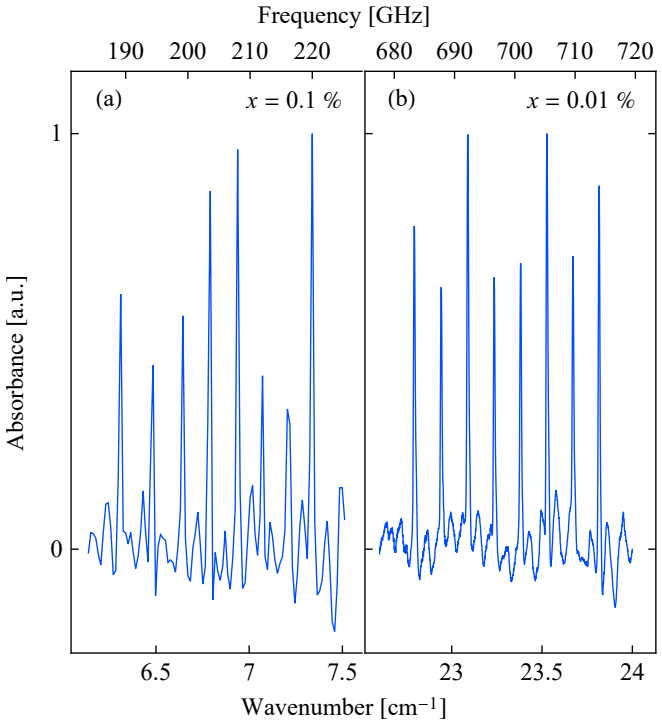

FIG. 2. Absorbance spectra of $LiY_{1-x}Ho_xF_4$ of (a) the $8.1 \rightarrow 8.2$ (TDS, $x = 0.1\%$, $T = 3\,\mathrm{K}$) and (b) the $8.1 \rightarrow 8.3$ (FTIR, $x = 0.01\%$, $T = 3.5\,\mathrm{K}$) transitions with conserved m_z.

terms in A_J and first-order term in B, all leading to corrections $\propto m_z^2$. These corrections determine the relative order of the m_z states within a singlet; note that for the states 8.2 and 8.3, the relative order is reversed. The dominant correction due to the small energy denominator in Eq. (3) comes from the mutual repulsion of these singlets caused by the dipolar HF interaction. An illustration of the HF levels of the 8.2 and 8.3 states is shown in Fig. 4.

B. Experiments

We measure the transmission of the $8.1 \rightarrow 8.2$ magnetic dipole transition in $LiY_{1-x}Ho_xF_4$ ($x = 0.1\%$) at a temperature of $T = 2.9\,\mathrm{K}$ by TDS with an instrument resolution of $0.017\,\mathrm{cm}^{-1}$ (500 MHz). The absorbance is shown in Fig. 2(a), where we directly resolve an eight-fold, approximately equidistant HF splitting of $\sim 0.146\,\mathrm{cm}^{-1}$ (4.4 GHz), which reflects the dominant linear HF shift of the ground state doublet 8.1. The deviation of the individual line intensities from a Boltzmann distribution (*cf.* Refs. [19, 20]) originates from sample- and setup-specific systematic errors such as residual interference of optical components. The extracted Gaussian full-width-at-half-maximum (FWHM) of a single HF line is $0.017 \pm 0.001\,\mathrm{cm}^{-1}$ (510 ± 30 MHz) and thus instrument-resolution limited.

The absorbance of the $8.1 \rightarrow 8.3$ magnetic dipole transition of $LiY_{1-x}Ho_xF_4$ ($x = 0.01\%$) was measured at $T = 3.5\,\mathrm{K}$ with FTIR spectroscopy and $0.001\,\mathrm{cm}^{-1}$(30 MHz) resolution. The absorbance spectrum is shown in Fig. 2(b), also revealing the eight-fold CF level splitting. The HF lines are nearly equidistant with a spacing of $\sim 0.146\,\mathrm{cm}^{-1}$ ($\sim 4.4\,\mathrm{GHz}$). The ultra-high resolution of the FTIR spectrometer allows for a closer inspection of a single HF line. Figure 3 shows the sixth HF peak at $23.527 \pm 0.001\,\mathrm{cm}^{-1}$ ($705.32 \pm 0.03\,\mathrm{GHz}$) in more detail. An asymmetry towards larger wavenumbers is apparent, which is best explained by the isotopic splitting effect due to the natural abundance of ^{6}Li (7.6%) and ^{7}Li (92.4%). It was shown that if a number ι of lighter ^{6}Li atoms substitute the more abundant ^{7}Li in the immediate neighborhood of a Ho^{3+} ion, the CF parameters will be slightly shifted due to two possible mechanisms: virtual phonon exchanges between CF states and local lattice deformations [26, 35, 36]. In particular, Ref. [36] has shown that the latter effect is dominant in $LiY_{1-x}Ho_xF_4$. The anharmonicity of the lattice vibrations leads to an effective repulsion of the lighter ^{6}Li isotopes from their nearest neighbors due to the change in the mass as compared to ^{7}Li. As a consequence, the F ions are shifted in position. Thus, whenever a ^{6}Li is near a Ho^{3+} ion, its CF is slightly changed and its energy shifted. This leads to additional peaks in the absorbance spectrum from Ho^{3+} ions with the number ι of less abundant ^{6}Li neighbors. Peaks associated with $\iota > 1$ or due to substitutions of more distant neighbors are too weak to be resolved. Thus, we only take the two strongest peaks $\iota = \{0, 1\}$ into account. By fitting two Gaussians, we find an isotopic splitting of $0.0098 \pm 0.0004\,\mathrm{cm}^{-1}$ (294 ± 12 MHz) and a Gaussian FWHM of $0.0090 \pm 0.0001\,\mathrm{cm}^{-1}$ (270 ± 3 MHz) for the individual peaks with the errors extracted from the covariance matrix. These findings are in agreement with the previously reported values of $0.0105 \pm 0.0015\,\mathrm{cm}^{-1}$ (315 ± 45 MHz)[26] and the calculations in Ref. [36]. HF line energies of the $8.1 \rightarrow 8.3$ transition are always referred to the center of the dominant $\iota = 0$ peak.

Next we completed FTIR measurements of the $8.2 \rightarrow 8.3$ magnetic dipole transition of $LiY_{1-x}Ho_xF_4$ ($x = 0.01\%$) with $0.002\,\mathrm{cm}^{-1}$ (60 MHz) resolution. The temperature was set to $T = 9\,\mathrm{K}$ to thermally populate the 8.2 state. The inset of Fig. 4 shows the respective absorbance with a Lorentzian fit. The HF corrections $\propto m_z^2$ in Eq. (3) lead to an observable difference in the transition energies of the individual m_z states. The HF levels are also illustrated (not to scale) in Fig. 4. We fit the absorbance spectrum of the $8.2 \rightarrow 8.3$ transition with four Lorentzian profiles, taking the degeneracy of $\pm m_z$ into account. We allowed for different intensities and peak frequencies, but imposed an identical linewidth, which we found to be $0.013 \pm 0.001\,\mathrm{cm}^{-1}$ (390 ± 30 MHz). Beyond a $0.008\,\mathrm{cm}^{-1}$ (240 MHz) constant offset, we obtain results that are consistent with the difference measured at the $8.1 \rightarrow 8.3$ and $8.1 \rightarrow 8.2$ transitions. We attribute the offset partly to the lower resolution of the

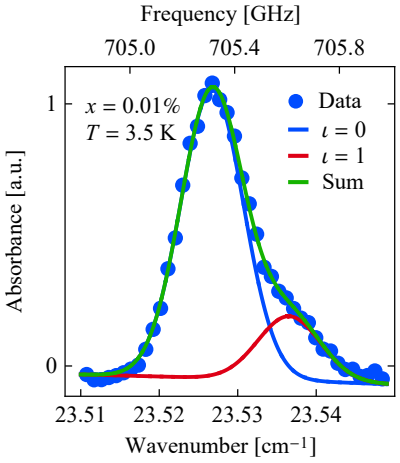

FIG. 3. Close-up of the asymmetric sixth $8.1 \rightarrow 8.3$ HF peak of $LiY_{1-x}Ho_xF_4$ ($x = 0.01\%$) at $T = 3.5\,K$. The green line is a fit to the main peak (blue), attributed to the majority of Ho ions having $\iota = 0$ ^{6}Li neighbors, and the smaller second peak (red) that is shifted by isotopic splitting due to $\iota = 1$ ^{6}Li neighbors. A sinusoidal background owing to interference effects was subtracted w.r.t. the data shown in Fig. 2.

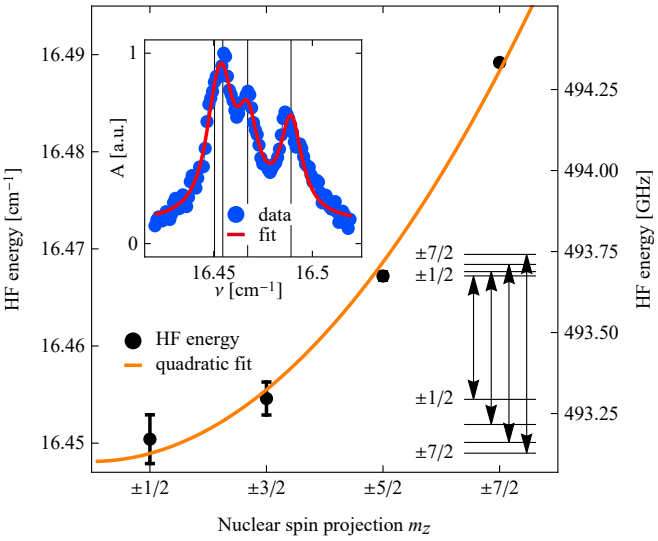

FIG. 4. HF shifts of the $8.2 \rightarrow 8.3$ transition as a function of the nuclear spin m_z. The shifts depend quadratically on m_z, as evidenced by the fit (orange). Note the degeneracy of $\pm m_z$ (see Table I). The top left inset shows the $8.2 \rightarrow 8.3$ absorbance raw data of $LiY_{1-x}Ho_xF_4$ ($x = 0.01\%$) at $T = 9\,K$ (blue) and a fit to Lorentzian profiles (red). The vertical lines denote the peak center positions and correspond to the data in the main figure. Also shown on the bottom right is the energy level diagram of the four observable $8.2 \rightarrow 8.3$ HF-split CF transitions.

Index	m_z	$8.1^+ \rightarrow 8.2$		$8.1^+ \rightarrow 8.3$		$8.2 \rightarrow 8.3$	
		[cm^{-1}]	[GHz]	[cm^{-1}]	[GHz]	[cm^{-1}]	[GHz]
1	−7/2	7.33	219.75	23.815	713.96	16.489	494.33
2	−5/2	7.21	216.15	23.671	709.64	16.467	493.67
3	−3/2	7.08	212.25	23.527	705.32	16.455	493.31
4	−1/2	6.94	208.06	23.381	700.94	16.450	493.16
5	+1/2	6.80	203.86	23.235	696.57	16.450	493.16
6	+3/2	6.64	199.06	23.088	692.16	16.455	493.31
7	+5/2	6.48	194.27	22.941	687.75	16.467	493.67
8	+7/2	6.31	189.17	22.794	683.35	16.489	494.33

TABLE I. HF split transition frequencies for CF level transitions $8.1 \rightarrow 8.2$ ($x = 0.1\%$), $8.1 \rightarrow 8.3$ ($x = 0.01\%$) and $8.2 \rightarrow 8.3$ ($x = 0.01\%$). All data are given in units of cm^{-1}and GHz. Uncertainties correspond to $\leq \pm 0.01$ (300), $\leq \pm 0.001$ (30) and $\leq \pm 0.003\,cm^{-1}$ (90 MHz) for the $8.1 \rightarrow 8.2$, $8.1 \rightarrow 8.3$ and $8.2 \rightarrow 8.3$ transitions, respectively.

TDS setup ($0.017\,cm^{-1}$, 510 GHz) and systematic differences between the two experimental setups.

In Table I, we summarize the individual HF transition energies which are in agreement with literature values (which, however, average over the individual HF transitions) [19, 20, 23, 26, 27]. Note that the $8.1 \rightarrow 8.3$ ($x = 0.1\%$) transitions, obtained with FTIR, exhibit smaller uncertainties than the $8.1 \rightarrow 8.2$ ($x = 0.01\%$) transitions, since the latter was measured with lower instrument resolution of the TDS setup. Owing to the significant line overlap of the $8.2 \rightarrow 8.3$ ($x = 0.01\%$) transition data, the respective uncertainties extracted from the fit covariance matrix amount to $\leq 0.003\,cm^{-1}$(90 MHz). Reference [37] shows that increasing the rare-earth concentrations up to 10% does not noticeably affect the CF energies, which justifies a direct comparison of the $x = 0.01\%$ and 0.1% CF energies.

IV. EXTRACTION OF CRYSTAL FIELD PARAMETERS AND HYPERFINE INTERACTIONS

The CF parameters of $LiY_{1-x}Ho_xF_4$ have been estimated previously based on CF level energies obtained as an average over their HF structure due to the limited resolution [19, 26, 29, 38, 39], or by magnetic susceptibility measurements [40–42]. We improve on those earlier results by including the individually-resolved HF energies of all three CF transitions reported here and supplement these data with results from higher-lying CF states from Ref. [20]. We fit the CF parameters and the HF coupling constant A_J simultaneously by numerically calculating the transition energies from the CF Hamiltonian (without HF interaction), as well as the HF splitting to first order in A_J. The transition energies are weighted with their measurement errors. This procedure only neglects small second-order corrections to the CF energies due to HF interactions, see Eqs. (2) and (3). The refined CF parameters are reported in Table II, and we extract the HF coupling constant $A_J = 0.02703 \pm 0.00003\,cm^{-1}$ (810.3 ± 0.9 MHz) in agreement with previous estimates in the literature of $A_J = 0.0282 \pm 0.0005$ [17] and $0.0270 \pm 0.0003\,cm^{-1}$ [43]. The error bars of the CF parameters and A_J are computed from the covariance

CF parameter	Energy [cm^{-1}]	[Hz]
B_2^0	$(-2.66 \pm 0.05) \times 10^{-1}$	$(-7.97 \pm 0.15) \times 10^{9}$
B_4^0	$(1.68 \pm 0.04) \times 10^{-3}$	$(5.04 \pm 0.12) \times 10^{7}$
B_4^4	$(2.81 \pm 0.02) \times 10^{-2}$	$(8.42 \pm 0.06) \times 10^{8}$
B_6^0	$(5.74 \pm 0.18) \times 10^{-6}$	$(1.72 \pm 0.54) \times 10^{5}$
B_6^4	$(5.60 \pm 0.03) \times 10^{-4}$	$(1.68 \pm 0.01) \times 10^{7}$
B_6^{-4}	$(0.00 \pm 3.84) \times 10^{-3}$	$(0.00 \pm 1.15) \times 10^{8}$

TABLE II. CF parameters extracted from the transition energy measurements. B_4^{-4} is set to be zero [42].

CF state	Energy [cm^{-1}]	[THz]	Symmetry	$\langle J_z \rangle = \mu/(g_J \mu_B)$
8.1	0.00	0.000	$\Gamma_{3,4}$	5.40
8.2	6.84	0.205	Γ_2	
8.3	23.31	0.699	Γ_2	
8.4	47.60	1.427	Γ_1	
8.5	56.92	1.706	Γ_1	
8.6	72.10	2.162	$\Gamma_{3,4}$	−3.59
8.7	190.88	5.722	Γ_1	
8.8	257.47	7.719	$\Gamma_{3,4}$	−2.30
8.9	275.31	8.254	Γ_2	
8.10	275.38	8.256	Γ_1	
8.11	288.66	8.654	Γ_1	
8.12	294.65	8.833	$\Gamma_{3,4}$	4.51
8.13	303.37	9.095	Γ_2	

TABLE III. Calculated energy levels of Ho^{3+} in $LiY_{1-x}Ho_xF_4$ based on the CF parameters shown in Table II. The last column shows the expectation value J_z of the magnetic Γ_4 states, which is proportional to their longitudinal magnetic moment μ and the Landé $g-$factor $g_J = 5/4$.

matrix.

A comparison of our CF parameter values in Table II with previous results shows that we predict generally smaller values, and we obtain significantly smaller values for B_2^0 and B_4^0. We attribute these corrections to the inclusion of the HF interaction term (to first order in A_J) in the Hamiltonian. In particular, fitting the HF structure allows us to use the magnetic moment of the 8.1 and 8.6 doublets (measured in Ref. [20]) as an additional constraint on the CF parameters, which determines the first order HF splitting. With the derived CF parameters we find a considerably ($\sim 10\%$) smaller magnetic moment $\mu/\mu_B = \pm 4.49$ of the 8.6 states than with previous CF parameters. We show the computed CF energies of the $^5I_8$ manifold and their magnetic moments in Table III. Compared to earlier reports, we find $2-10\%$ deviations for the predicted energies of the CF levels 8.7 to 8.13.

In contrast to A_J, the determination of the quadrupolar HF interaction constant B requires precise knowledge of the deviations from the linear dipolar HF contributions. We utilize our high-resolution spectra (8.1 → 8.2, 8.1 → 8.3, 8.2 → 8.3) to fit B separately, by using the determined CF parameters and A_J, and numerically calculating the full HF spectrum. We find

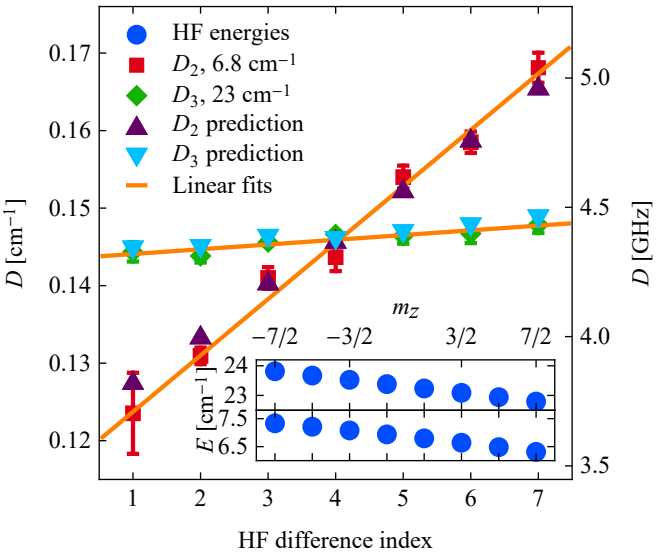

FIG. 5. Energy differences D_2 (red) and D_3 (green) between neighboring HF transitions, shown as a function of the HF index. Linear fits to the experimental data are shown in orange. The respective slopes $s_{2,3}$ are a measure of the HF corrections $\propto m_z^2$. The numerical calculations based on our fitted CF parameters are shown in violet and cyan. The HF transition energies are shown in the inset for the 8.1 → 8.2 and 8.1 → 8.3 transition in the upper and lower panel, respectively.

$B = 0.04 \pm 0.01\,\mathrm{cm}^{-1}$ ($1.2 \pm 0.3\,\mathrm{GHz}$), which is comparable to the literature value $B = 0.059\,\mathrm{cm}^{-1}$ (1.8 GHz) calculated from the free Ho atom [22].

The parameters A_J and B allow us to numerically compute the HF spectrum. We present a comparison to the experimental data in Fig. 5. To emphasize the HF corrections $\propto m_z^2$, we look at the difference D_n of transition frequencies 8.1 → 8.n between neighboring m_z for $n = 2, 3$. From Eqs.(2, 3) we expect $D_{2,3}$ to be linear in m_z, with the slopes being a measure of the HF corrections $\propto m_z^2$. We find the slopes of $D_{2,3}$ (orange lines) to be $s_2 = (7.2 \pm 0.5) \times 10^{-3}\,\mathrm{cm}^{-1}$ ($215 \pm 15\,\mathrm{MHz}$) and $s_3 = (6 \pm 1) \times 10^{-4}\,\mathrm{cm}^{-1}$ ($18 \pm 3\,\mathrm{MHz}$), respectively, based on a linear regression. The numerically calculated values are shown in violet (D_2) and cyan (D_3). On average, we find the deviations of the experimental and numerically calculated values to be 16% for the 8.2 and only 1.5% for the 8.3 level, respectively. The error reflects the respective measurement resolutions.

The experimental values of D_2 and D_3 allow an order-of-magnitude estimation of the m_z^2-correction of the ground state (with the prefactor $\lambda_1/2$), even without precise knowledge of the CF and HF parameters. We provide a detailed derivation thereof in the Appendix B 2. Namely, we neglect the quadrupolar interaction B and restrict the sum over the CF states in Eqs. (2, 3) to the three lowest CF states, which contribute the most to the correction. We then exploit the anti-symmetry of the second-order corrections between the 8.1, 8.2 and

8.3 states to extract $\lambda_1 = (s_1 + s_2)/4 = (2.0 \pm 0.2) \times 10^{-3}\,\mathrm{cm}^{-1}$ (60±6 MHz) from our data, *cf.* Eq. (B5). This is in agreement with the numerical calculation, yielding $\lambda_1 = 0.0024\,\mathrm{cm}^{-1}$ (72 MHz). Based on the errors found for the 8.2 and 8.3 energy level predictions, we expect a similar error of $\lesssim 16\%$ for λ_1. Akin to λ_1, we estimate $\lambda_2 = (-2.5 \pm 0.1) \times 10^{-3}\,\mathrm{cm}^{-1}$ (-75 ± 3 MHz) and $\lambda_3 = (1.9 \pm 0.3) \times 10^{-3}\,\mathrm{cm}^{-1}$ (57 ± 9 MHz) by also including the $8.2 \rightarrow 8.3$ transition. Both values are also in agreement with the numerical results $\lambda_2 = -0.0040\,\mathrm{cm}^{-1}$ (-120 MHz) and $\lambda_3 = 0.0017\,\mathrm{cm}^{-1}$ (51 MHz).

These m_z^2-corrections, *i.e.* λ_n, have direct implications on the possibility to unambiguously address HF states. Direct addressing of HF transitions is of general importance to engineer an out-of-equilibrium population in HF levels *e.g.* in the context of pseudo-cold ground states (see Ref. [44] and references therein) or encoding quantum information into HF states. Specifically, a single $m_z \rightarrow m_z + 1$ transition within an electronic CF state $|8.n\rangle$ can only be driven if the HF line width is smaller than λ_n, which is the frequency difference of neighboring $m_z \rightarrow m_z + 1$ transitions. The same holds true for m_z-conserving transitions between singlet-symmetry CF states (*e.g.* $8.2 \rightarrow 8.3$). At first sight, the line widths of our spectra seem not to satisfy this criterion. However, a quantitative evaluation of contributions to the line width is necessary to assess whether a regime (temperature, Ho-doping, etc.) for a specific CF state exists, where unambiguous addressing of HF states is possible [45]. This problem can be circumvented by driving protocols involving another excited doublet CF level [46]. Nuclear states can then be manipulated via a first m_z-conserving transition to an excited doublet with a subsequent transition to the m_z+1 state in the original CF level. For such manipulations involving a nuclear spin flip, the transition energies with different m_z differ already in their first order hyperfine correction and do not rely on the much smaller m_z^2-corrections λ. Our spectra (Fig. 2) show that doublet states in $LiY_{1-x}Ho_xF_4$ enable such two-step flips thanks to the sufficiently large first-order HF splitting.

V. CONCLUSIONS

We have extended the characterization of the ground CF state manifold of $LiY_{1-x}Ho_xF_4$ ($x = 1\%$, 0.1%, and 0.01%) by direct optical measurements of transitions within the lowest three CF states. From the data we have calculated the CF parameters, which differ from previous estimates because our refinement also considers the magnetic moments of the CF states as an additional fit constraint via the first order HF shift in A_J. This enabled us to deduce the dipolar HF constant $A_J = 0.02703 \pm 0.00003\,\mathrm{cm}^{-1}$ (810.3 ± 0.9 MHz) by purely optical means. Using the CF parameters we predict the energies for the CF states of the ${}^5I_8$ ground state manifold. Our high measurement resolution allowed us to determine the quadrupolar HF constant $B = 0.04 \pm 0.01\,\mathrm{cm}^{-1}$ (1.2 ± 0.3 GHz) and subsequently to calculate the HF corrections of the three lowest CF states. We directly corroborated these calculations via estimations from our data. Further, we report in Appendix A the far-infrared refractive index of $LiY_{1-x}Ho_xF_4$.

We have quantified the low energy second order HF corrections λ_n in $LiY_{1-x}Ho_xF_4$ which impose restrictions on the linewidth of the respective states for unambiguous addressing of HF energy levels. The ultra-high resolution methods used here are obviously applicable to the characterization of other rare earth-based platforms for quantum science and technology. In the case of $LiY_{1-x}Ho_xF_4$, we have precisely determined the low-energy electronuclear Hamiltonian, thus providing a revised starting point both for state manipulation using THz radiation as well as for detailed understanding of the effects of external fields, most notably the mapping to the simple transverse field Ising model, across the entire dilution series.

ACKNOWLEDGMENTS

FTIR spectroscopy data was taken at the X01DC beamline of the Swiss Light Source, Paul Scherrer Institut, Villigen, Switzerland. We thank H. M. Rønnow, P. Babkevich and J. Bailey for helpful discussions and experimental support. We thank S. Stutz for technical support at the X01DC beamline. We acknowledge financial support by the Swiss National Science Foundation, Grant No. 200021_166271, the European Research Council under the European Union's Horizon 2020 research and innovation programme HERO (Grant agreement No. 810451), and the Engineering and Physical Sciences Research Council, U.K. ('HyperTerahertz' EP/P021859/1 and 'COTS' EP/J017671/1).

Appendix A: Refractive index in the far-infrared

We report the frequency-dependent ordinary refractive index n_o of $LiY_{1-x}Ho_xF_4$ in the FIR regime $10 \lesssim \tilde{\nu} \lesssim 70\,\mathrm{cm}^{-1}$. Figure 6 shows $n_o(\nu)$ of a 2.07 mm thick $x = 1\%$ crystal for $T = 100$ and 6 K, as measured with TDS, where the THz electric field is polarized perpendicular to the crystallographic $c-$axis (the optic axis lies along crystallographic $c-$axis). The results have been obtained from the complex transmission of the sample, calculated from the Fourier transforms of the measured time-domain signals with and without the crystal in the cryostat. The index is then given by $n = c \times \delta\phi/(\omega L) + n_{\mathrm{air}}$, where c is the speed of light, ω the angular frequency, L is the thickness of the sample, $n_{\mathrm{air}} = 1$ is the refractive index of air and $\delta\phi$ is the phase difference, obtained from the complex transmission. We fit a phenomenological model $n_o(\tilde{\nu}) = a/(\tilde{\nu} - \tilde{\nu}_0) + c$ to the data, motivated by the divergence of the refractive

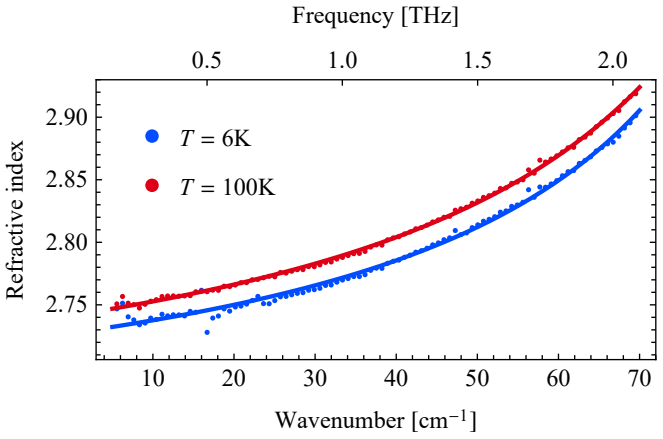

FIG. 6. Ordinary refractive index of $LiY_{1-x}Ho_xF_4$ ($x = 1\%$) measured at temperatures of $T = 100$ and 6 K shown in red and blue, respectively. Solid lines are fits to the data of the phenomenological model described in the main text.

index near zone-center phonons around $\tilde{\nu}_0 = 150\,\mathrm{cm}^{-1}$ [47]. From a least squares fit we find $c = 2.62 \pm 0.01$ for both temperatures, $a_{6\mathrm{K}} = -11.1 \pm 0.9\,\mathrm{cm}^{-1}$, $a_{100\mathrm{K}} = -13.5 \pm 0.5\,\mathrm{cm}^{-1}$, $\tilde{\nu}_{0,6\mathrm{K}} = 110 \pm 2\,\mathrm{cm}^{-1}$ and $\tilde{\nu}_{0,100\mathrm{K}} = 115 \pm 1\,\mathrm{cm}^{-1}$.

Appendix B: Hyperfine energies

1. Perturbation theory

The dipolar and quadrupolar HF interaction Hamiltonian is given in Eq. (1). Rewriting this Hamiltonian in terms of the operators J_z, J_+, J_- and I_z, I_+, I_-, allows us to derive the perturbative second-order energy corrections in A_J and first-order ones in B as

$$\begin{aligned}\delta_{8.n^\sigma,m_z} = & A_J \langle 8.n^\sigma|J_z|8.n^\sigma\rangle m_z \\ & + \sum_{j\neq i}\sum_{\sigma'=\pm}\frac{A_J^2}{\Delta E_{ij}}\Big[|\langle 8.j^\sigma|J_z|8.n^\sigma\rangle|^2 m_z^2 \\ & + \frac{1}{4}|\langle 8.j^{\sigma'}|J_-|8.n^\sigma\rangle|^2\big(I(I+1)-m_z(m_z+1)\big) \\ & + \frac{1}{4}|\langle 8.j^{\sigma'}|J_+|8.n^\sigma\rangle|^2\big(I(I+1)-m_z(m_z-1)\big)\Big] \\ & + \frac{B\langle 8.n^\sigma|3J_z^2-J(J+1)|8.n^\sigma\rangle}{4I(2I-1)J(2J-1)}(3m_z^2-I(I+1)).\end{aligned} \tag{B1}$$

We have already used here that owing to the S_4 crystal symmetry of $LiYF_4$, the expectation value of the angular momentum operators with the CF states can only be non-zero for the J_z component, and similarly only the J_z^2 component of the quadrupol operators.

The S_4 and time-reversal symmetries simplify the expression (B1) even further, since most of the matrix elements vanish. Due to time-reversal symmetry, the first order correction in A_J is only non-zero for CF doublets, *e.g.*, levels 8.1 and 8.6. Owing to the S_4 crystal symmetry (with the symmetry operator being $U = \exp\left(i\frac{\pi}{4}J_z\right)$), the matrix elements $\langle 8.j^{\sigma'}|J_z|8.i^\sigma\rangle$ of the second-order corrections in A_J are finite only if the states $|8.i\rangle$ and $|8.j\rangle$ carry the same irreducible representation. Furthermore, $\langle 8.i^\sigma|J_+|8.j^{\sigma'}\rangle$ is non-zero only for matrix elements between pairs of states $\langle\Gamma_1|J_+|\Gamma_3\rangle$, $\langle\Gamma_3|J_+|\Gamma_2\rangle$, $\langle\Gamma_2|J_+|\Gamma_4\rangle$, $\langle\Gamma_4|J_+|\Gamma_1\rangle$, and—with i and j exchanged—for the Hermitian conjugate matrix elements $\langle 8.i^\sigma|J_+|8.j^{\sigma'}\rangle^\dagger = \langle 8.j^{\sigma'}|J_-|8.i^\sigma\rangle$ as $J_- = J_+^\dagger$. Here, $|\Gamma_i\rangle$ stands for any CF state that transforms as Γ_i. Using these symmetry constraints in Eq. (B1), we arrive at Eqs. (2) and (3).

2. Extraction of the ground state HF corrections

In the following we restrict the sum over CF states in Eq. (B1) to the lowest three CF states 8.1, 8.2 and 8.3. This is motivated by the fact that these states give the dominant contributions in the second-order corrections of A_J due to the small energy denominators. Further, we neglect the quadrupolar coupling B, which enables us to estimate the ground state HF energies from our data without prior knowledge of the CF parameters or the constant A_J.

Taking into account this reduced Hilbert space of only the three lowest CF states, the energy corrections $\delta_{8.i^\sigma,m_z}$ up to second order in A_J can be written as

$$\begin{aligned}\delta_{8.1^+,m_z} =& \delta_{8.1^-,-m_z} \\ =& K_{1,1}(m_z) + K_{1,2}(m_z) + K_{1,3}(m_z), \\ \delta_{8.2,\pm m_z} =& K_{2,3}(m_z) + 2K_{2,1}(m_z), \\ \delta_{8.3,\pm m_z} =& K_{3,2}(m_z) + 2K_{3,1}(m_z),\end{aligned} \tag{B2}$$

where $K_{i,j}$ defines the perturbative energy correction of level i due to the level j

$$\begin{aligned}K_{1,1}(m_z) =& A_J\langle 8.1^+|J_z|8.1^+\rangle m_z, \\ K_{1,i=2,3}(m_z) =& \frac{A_J^2}{4}\frac{|\langle 8.i|J_-|8.1^+\rangle|^2}{\Delta E_{1i}} \\ & \times\big(I(I+1)-m_z(m_z+1)\big), \\ K_{2,3}(m_z) =& \frac{A_J^2|\langle 8.3|J_z|8.2\rangle|^2}{\Delta E_{23}}m_z^2, \\ K_{i,j\neq i}(m_z) =& -K_{j,i}(m_z).\end{aligned} \tag{B3}$$

Measuring transitions between the 8.1, 8.2 and 8.3 states (with m_z conserved) allows us to extract the second-order ground state HF corrections in A_J, *i.e.* $K_{1,2}(m_z) + K_{1,3}(m_z)$. We use the anti-symmetry of $K_{i,j\neq i}(m_z)$ in Eq. (B3) to cancel out the contributions $K_{2,3}(m_z)$ in the transition frequencies. We do this by using the differences $D_i(m_z)$ ($i = 2, 3$) of transition frequencies $8.1 \to 8.i$ between neighboring m_z

$$\begin{aligned}D_i(m_z) =& (\delta_{8.i,m_z+1} - \delta_{8.1^+,m_z+1}) \\ & - (\delta_{8.i,m_z} - \delta_{8.1^+,m_z}).\end{aligned} \tag{B4}$$

The purely electronic CF transition energies cancel out in $D_i(m_z)$ when we take the difference of two transitions. We add $D_2(m_z)$ and $D_3(m_z)$ to eliminate the contributions $K_{2,3}(m_z)$ and $K_{3,2}(m_z)$ (due to the antisymmetry of K). Taking the difference between neighboring m_z, we recover the coefficient of the $\propto m_z^2$ correction in Eqs. (B2, B3). We introduce λ_1 which is twice this coefficient:

$$\begin{aligned}\lambda_1 =&\frac{\mathrm{d}\delta_{8.1^+,m_z}}{\mathrm{d}m_z} = \frac{\mathrm{d}}{\mathrm{d}m_z}(K_{1,2}(m_z)+K_{1,3}(m_z))\\ =&-\frac{1}{4}\big[D_2(m_z+1)+D_3(m_z+1)\\ &-(D_2(m_z)+D_3(m_z))\big].\end{aligned} \tag{B5}$$

The energy difference between neighboring $m_z \to m_z+1$ transitions within the ground state doublet is given by λ_1. Its value is estimated in the main text by fitting linear functions to $D_i(m_z)$.

Similarly, we determine the coefficients of the m_z^2-HF-correction in the 8.2 and 8.3 states, λ_2 and λ_3, respectively, as

$$\begin{aligned}\lambda_2 =&\frac{1}{4}\big[D_2(m_z+1)+D_3(m_z+1)-2D_1(m_z+1)\\ &-(D_2(m_z)+D_3(m_z)-2D_2(m_z+1))\big],\end{aligned} \tag{B6}$$

and

$$\begin{aligned}\lambda_3 =&\frac{1}{4}\big[D_2(m_z+1)+D_3(m_z+1)+2D_1(m_z+1)\\ &-(D_2(m_z)+D_3(m_z)+2D_2(m_z+1))\big],\end{aligned} \tag{B7}$$

where we defined the differences $D_1(m_z)$ of transition frequencies $8.2 \to 8.3$ between neighboring m_z as

$$D_1(m_z) = (\delta_{8.3,m_z+1}-\delta_{8.2,m_z+1})-(\delta_{8.3,m_z}-\delta_{8.2,m_z}). \tag{B8}$$

[1] R. Giraud, W. Wernsdorfer, A. M. Tkachuk, D. Mailly, and B. Barbara, Nuclear spin driven quantum relaxation in $LiY_{0.998}Ho_{0.002}F_4$, Phys. Rev. Lett. **87**, 057203 (2001).

[2] H. M. Rønnow, R. Parthasarathy, J. Jensen, G. Aeppli, T. F. Rosenbaum, and D. F. McMorrow, Quantum phase transition of a magnet in a spin bath, Science **308**, 389 (2005).

[3] D. Bitko, T. F. Rosenbaum, and G. Aeppli, Quantum critical behavior for a model magnet, Phys. Rev. Lett. **77**, 940 (1996).

[4] W. Wu, B. Ellman, T. F. Rosenbaum, G. Aeppli, and D. H. Reich, From classical to quantum glass, Phys. Rev. Lett. **67**, 2076 (1991).

[5] C. Ancona-Torres, D. M. Silevitch, G. Aeppli, and T. F. Rosenbaum, Quantum and classical glass transitions in $LiHo_xY_{1-x}F_4$, Phys. Rev. Lett. **101**, 057201 (2008).

[6] W. Wu, D. Bitko, T. F. Rosenbaum, and G. Aeppli, Quenching of the nonlinear susceptibility at a T=0 spin glass transition, Phys. Rev. Lett. **71**, 1919 (1993).

[7] J. Brooke, T. F. Rosenbaum, and G. Aeppli, Tunable quantum tunnelling of magnetic domain walls, Nature **413**, 610 (2001).

[8] D. M. Silevitch, D. Bitko, J. Brooke, S. Ghosh, G. Aeppli, and T. F. Rosenbaum, A ferromagnet in a continuously tunable random field, Nature **448**, 567 (2007).

[9] S. Ghosh, T. F. Rosenbaum, G. Aeppli, and S. N. Coppersmith, Entangled quantum state of magnetic dipoles, Nature **425**, 48 (2003).

[10] S. Ghosh, R. Parthasarathy, T. F. Rosenbaum, and G. Aeppli, Coherent spin oscillations in a disordered magnet, Science **296**, 2195 (2002).

[11] M. A. Schmidt, D. M. Silevitch, G. Aeppli, and T. F. Rosenbaum, Using thermal boundary conditions to engineer the quantum state of a bulk magnet, Proc. Natl. Acad. Sci. U.S.A. **111**, 3689 (2014).

[12] D. M. Silevitch, C. Tang, G. Aeppli, and T. F. Rosenbaum, Tuning high$-Q$ nonlinear dynamics in a disordered quantum magnet, Nat. Commun. **10**, 4001 (2019).

[13] J. Brooke, D. Bitko, F. T. Rosenbaum, and G. Aeppli, Quantum annealing of a disordered magnet, Science **284**, 779 (1999).

[14] A. Dutta, G. Aeppli, B. Chakrabarti, U. Divakaran, T. Rosenbaum, and D. Sen, *Quantum Phase Transitions in Transverse Field Models* (Cambridge University Press, 2015).

[15] H. Kjønsberg and S. M. Girvin, The classical phase transition in $LiHoF_4$: Results from mean field theory and monte carlo simulations, AIP Conference Proceedings **535**, 323 (2000).

[16] P. B. Chakraborty, P. Henelius, H. Kjønsberg, A. W. Sandvik, and S. M. Girvin, Theory of the magnetic phase diagram of $LiHoF_4$, Phys. Rev. B **70**, 144411 (2004).

[17] J. Magariño, J. Tuchendler, P. Beauvillain, and I. Laursen, EPR experiments in $LiTbF_4$, $LiHoF_4$, and $LiErF_4$ at submillimeter frequencies, Phys. Rev. B **21**, 18 (1980).

[18] K. Kjaer, J. Als-Nielsen, I. Laursen, and F. K. Larsen, A neutron scattering study of the dilute dipolar-coupled ferromagnets $LiTb_{0.3}Y_{0.7}F_4$ and $LiHo_{0.3}Y_{0.7}F_4$ structure, magnetisation and critical scattering, J. Condens. Matter Phys. **1**, 5743 (1989).

[19] P. Babkevich, A. Finco, M. Jeong, B. Dalla Piazza, I. Kovacevic, G. Klughertz, K. W. Krämer, C. Kraemer, D. T. Adroja, E. Goremychkin, T. Unruh, T. Strässle, A. Di Lieto, J. Jensen, and H. M. Rønnow, Neutron spectroscopic study of crystal-field excitations and the effect of the crystal field on dipolar magnetism in $LiRF_4$ (R=Gd, Ho, Er, Tm, and Yb), Phys. Rev. B **92**, 144422 (2015).

[20] G. Matmon, S. A. Lynch, T. F. Rosenbaum, A. J. Fisher, and G. Aeppli, Optical response from terahertz to visible light of electronuclear transitions in $LiYF_4 : Ho^{3+}$, Phys. Rev. B **94**, 205132 (2016).

[21] R. I. Hermans, J. Seddon, H. Shams, L. Ponnampalam, A. J. Seeds, and G. Aeppli, Ultra-high-resolution software-defined photonic terahertz spectroscopy, Optica **7**, 1445 (2020).

[22] B. Bleaney, *Magnetic Properties of Rare Earth Metals*, edited by R. J. Elliott (Springer US, Boston, MA, 1972).

[23] N. Agladze and M. Popova, Hyperfine structure in optical spectra of $LiYF_4$-Ho, Solid State Communications **55**, 1097 (1985).

[24] M. J. P. Gingras and P. Henelius, Collective phenomena in the $LiY_{1-x}Ho_xF_4$ quantum ising magnet: Recent progress and open questions, Journal of Physics: Conference Series **320**, 012001 (2011).

[25] S. Albert, K. K. Albert, P. Lerch, and M. Quack, Synchrotron-based highest resolution fourier transform infrared spectroscopy of naphthalene ($C_{10}H_8$) and indole (C_8H_7N) and its application to astrophysical problems, Faraday Discuss. **150**, 71 (2011).

[26] G. S. Shakurov, M. V. Vanyunin, B. Z. Malkin, B. Barbara, R. Y. Abdulsabirov, and S. L. Korableva, Direct measurements of anticrossings of the electron-nuclear energy levels in $LiYF_4 : Ho^{3+}$ with submillimeter EPR spectroscopy, Applied Magnetic Resonance **28**, 251 (2005).

[27] G. S. Shakurov, B. Z. Malkin, M. V. Vanyunin, and S. L. Korableva, Multi-range high-frequency EPR spectroscopy of $LiYF_4$ and $LiLuF_4$ crystals doped by rare-earth ions, Physics of the Solid State **50**, 1619 (2008).

[28] N. Karayianis, D. Wortman, and H. Jenssen, Analysis of the optical spectrum of Ho^{3+} in $LiYF_4$, Journal of Physics and Chemistry of Solids **37**, 675 (1976).

[29] H. P. Christensen, Spectroscopic analysis of $LiHoF_4$ and $LiErF_4$, Phys. Rev. B **19**, 6564 (1979).

[30] K. N. Boldyrev, M. N. Popova, B. Z. Malkin, and N. M. Abishev, Direct observation of hyperfine level anticrossings in the optical spectra of a $^7LiYF_4 : Ho^{3+}$ single crystal, Phys. Rev. B **99**, 041105(R) (2019).

[31] A. Beckert, H. Sigg, and G. Aeppli, Taking advantage of multiplet structure for lineshape analysis in fourier space, Opt. Express **28**, 24937 (2020).

[32] A. Abragam and B. Bleaney, *Electron Paramagnetic Resonance of Transition Ions*, International series of monographs on physics (Clarendon P., 1970).

[33] N. I. Agladze, E. A. Vinogradov, and M. N. Popova, Manifestation of quadrupole hyperfine interaction and of interlevel interaction in the optical spectrum of the $LiYF_4$: Ho crystal, JETP **64**, 716 (1986).

[34] M. N. Popova, E. P. Chukalina, B. Z. Malkin, and S. K. Saikin, Experimental and theoretical study of the crystal-field levels and hyperfine and electron-phonon interactions in $LiYF_4$:Er^{3+}, Phys. Rev. B **61**, 7421 (2000).

[35] N. I. Agladze, M. N. Popova, G. N. Zhizhin, V. J. Egorov, and M. A. Petrova, Isotope structure in optical spectra of $LiYF_4 : Ho^{3+}$, Phys. Rev. Lett. **66**, 477 (1991).

[36] N. I. Agladze, M. N. Popova, M. A. Koreiba, B. Z. Malkin, and V. R. Pekurovskii, Isotope effects in the lattice structure and vibrational and optical spectra of $^6Li_x^7Li_{1-x}YF_4$: Ho crystals, JETP **77**, 1021 (1993).

[37] F. Könz, Y. Sun, C. W. Thiel, R. L. Cone, R. W. Equall, R. L. Hutcheson, and R. M. Macfarlane, Temperature and concentration dependence of optical dephasing, spectral-hole lifetime, and anisotropic absorption in Eu^{3+}: Y_2SiO_5, Phys. Rev. B **68**, 085109 (2003).

[38] S. N. Gifeisman, A. M. Tkachuk, and V. V. Prizmak, Optical spectra of Ho^{3+} ion in $LiYF_4$ crystals, Optics and Spectroscopy **44**, 68 (1978).

[39] C. Görller-Walrand, K. Binnemans, and L. Fluyt, Crystal-field analysis of Eu^{3+} in $LiYF_4$, J. Condens. Matter Phys. **5**, 8359 (1993).

[40] P. E. Hansen, T. Johansson, and R. Nevald, Magnetic properties of lithium rare-earth fluorides: Ferromagnetism in $LiErF_4$ and$LiHoF_4$ and crystal-field parameters at the rare-earth and li sites, Phys. Rev. B **12**, 5315 (1975).

[41] P. Beauvillain, C. Chappert, and I. Laursen, Critical behaviour of the magnetic susceptibility at marginal dimensionality in $LiTbF_4$, Journal of Physics C: Solid State Physics **13**, 1481 (1980).

[42] H. M. Rønnow, J. Jensen, R. Parthasarathy, G. Aeppli, T. F. Rosenbaum, D. F. McMorrow, and C. Kraemer, Magnetic excitations near the quantum phase transition in the ising ferromagnet $LiHoF_4$, Phys. Rev. B **75**, 054426 (2007).

[43] G. Mennenga, L. de Jongh, and W. Huiskamp, Field dependent specific heat study of the dipolar ising ferromagnet $LiHoF_4$, Journal of Magnetism and Magnetic Materials **44**, 59 (1984).

[44] D. G. Cory, R. Laflamme, E. Knill, L. Viola, T. F. Havel, N. Boulant, G. Boutis, E. Fortunato, S. Lloyd, R. Martinez, C. Negrevergne, M. Pravia, Y. Sharf, G. Teklemariam, Y. S. Weinstein, and W. H. Zurek, Nmr based quantum information processing: Achievements and prospects, Fortschritte der Physik **48**, 875 (2000).

[45] A. Beckert, M. Grimm, M. Müller, H. Sigg, S. Gerber, G. Matmon, and G. Aeppli, Decoherence mechanisms of crystal field excitations in rare-earth low-concentration-doped crystals, unpublished (2021).

[46] M. Grimm, A. Beckert, G. Aeppli, and M. Müller, Universal quantum computing using electronuclear wavefunctions of rare-earth ions, PRX Quantum **2**, 010312 (2021).

[47] S. Salaün, M. T. Fornoni, A. Bulou, M. Rousseau, P. Simon, and J. Y. Gesland, Lattice dynamics of fluoride scheelites: I. Raman and infrared study of $LiYF_4$ and $LiLnF_4$ (Ln = Ho, Er, Tm and Yb), J. Condens. Matter Phys. **9**, 6941 (1997).